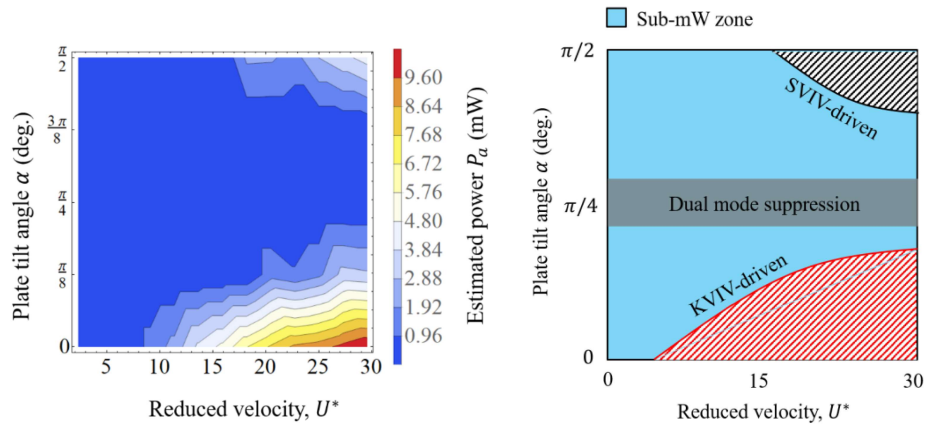


Graphical Abstract

Vortex-induced Vibration of an Angled Cruciform for Energy Harvesting

Ahmad Adzlan, Mohamed Sukri Mat Ali, Sheikh Ahmad Zaki



Highlights

Vortex-induced Vibration of an Angled Cruciform for Energy Harvesting

Ahmad Adzlan,Mohamed Sukri Mat Ali,Sheikh Ahmad Zaki

- Three main energy harvesting regimes were identified, based on the cruciform angle
- The streamwise-vortex induced vibration regime produces power in the order of 1 mW
- Power output is below 1 mW between angles 67.5° and 22.5°
- Power output can achieve up to 10 mW, as the angle is brought closer to 0° .

Vortex-induced Vibration of an Angled Cruciform for Energy Harvesting

Ahmad Adzlan^{a,b,*}, Mohamed Sukri Mat Ali^a and Sheikh Ahmad Zaki^a

^aMalaysia-Japan International Institute of Technology, Universiti Teknologi Malaysia, 54200 Kuala Lumpur, Malaysia

^bFaculty of Engineering, Universiti Malaysia Sarawak, 94300 Kota Samarahan, Sarawak, Malaysia

ARTICLE INFO

Keywords:

Vortex-induced vibration
Vibration energy harvester
CFD simulation
Streamwise vorticity
Ensemble empirical mode decomposition (EEMD)
Hilbert transform

ABSTRACT

We investigated the displacement and lift time series of a circular cylinder - strip plate cruciform system for energy harvesting in the Reynolds number range $1.1 \times 10^3 \leq Re \leq 14.6 \times 10^3$, numerically using the open source C++ library: OpenFOAM. The Karman vortex-induced vibration (KVIV) regime was identified between reduced velocity, U^* , 2.3 and 13.6, while the streamwise vortex-induced vibration (SVIV) regime was identified between $18.2 \leq U^* \leq 29.5$. We analysed the cylinder displacement and lift time series using the Hilbert-Huang transform (HHT). Within this range of U^* , Karman vortex shedding contributes nearly as much as streamwise vortex shedding to the root-mean-square amplitude of total lift, while between $25.0 \leq U^* \leq 29.5$, the Karman component contribution is on average twice that of the streamwise component. These findings hint at the possibility to improve the power output of the harvester by a factor of two between $18.2 \leq U^* \leq 22.7$ and by a factor of three between $25.0 \leq U^* \leq 29.5$, if we can unite the contribution to the root-mean-square amplitude of the total lift under a single vibration-driving mechanism: the shedding of streamwise vortex.

1. Introduction

Streamwise vortex-induced vibration (SVIV) is a type of vortex-induced vibration (VIV) driven by vortical structures whose vorticity vector points in the direction of the free stream. In recent decades, there have been efforts to exploit the SVIV phenomenon from cruciform structures for energy harvesting, an example of which is given in Fig. 1. The literature on this subject can be broadly categorised into two groups: how the mechanical properties of the oscillator (e.g., mass ratio, damping, etc.) affects the amplitude/frequency response of SVIV (Koide et al., 2009, 2013; Nguyen et al., 2012) and how the minutiae of the flow field affect the force driving the vibration of the cylinder, i.e. the fluid mechanical aspect of the system (Deng et al., 2007; Koide et al., 2017; Zhao and Lu, 2018).

In the first focus area, researchers studied some permutation of the following method to convert the vibration into electrical power. The method consists of a coil and magnet. The coil, which moves with the vibrating cylinder, creates relative motion against the magnet, which is placed in the hollow of the coil (Koide et al., 2009). While investigating the system at a Reynolds number in the order of $Re \sim O(10^4)$, Koide et al. (2009) showed that increased damping due to energy harvesting reduces the maximum vibration amplitude close to a factor of 4. Amplitude reduction due to increased total damping was also mentioned in Bernitsas et al. (2008); Bernitsas and Raghavan (2008); Bernitsas et al. (2009). Further investigation in Nguyen et al. (2012) revealed that damping not only affects the amplitude response of

*Corresponding author

 aafkhairi@graduate.utm.my (A. Adzlan); sukri.kl@utm.my (M.S.M. Ali); sheikh.kl@utm.my (S.A. Zaki)
ORCID(s): 0000-0003-0290-3185 (A. Adzlan); 0000-0001-6411-9965 (S.A. Zaki)

the cylinder but also narrows the synchronisation region between vortex shedding and cylinder vibration. Moreover, Nguyen et al. (2012) demonstrated a strong coupling between mass ratio and damping in determining both the width of the synchronisation region and the maximum amplitude response of the cylinder.

In the second focus area, investigators turned their attention to the details of the flow where streamwise vortex shedding occurs. One such study carefully shot motion pictures of the dye-injected flow (Koide et al., 2017) at Reynolds number in the order of $Re \sim O(10^3)$. A lower Reynolds number (Re) reduces the amount of turbulence in the flow, allowing a clearer shot of the vortex structures. Their study also highlights the higher level of turbulence produced by the circular cylinder-strip plate cruciform in contrast to the twin circular cylinder cruciform, which diminishes the periodicity of vortex shedding. Although visually enlightening, this and other more qualitative studies contribute little towards improving our understanding of the relationship between vortex shedding and the resulting lift. Deng et al. (2007) demonstrated a way to overcome such a shortcoming.

In their study, Deng et al. (2007) examined the flow field of a twin circular cylinder cruciform using computational fluid dynamics (CFD). Their domain stretches $28D$ in the streamwise direction, $16D$ in the transverse direction and $12D$ in the spanwise direction. They studied an Re range yet another order of magnitude smaller than that studied by Koide et al. (2017), possibly to get an even clearer visualisation of the vortical structures with less turbulence, and to ease computational requisites. At a fixed $Re = 150$, streamwise vortices form even at a gap ratio of 2. This result differs quite strikingly from Koide et al. (2006, 2007), conducted at an Re twice the order of magnitude of Deng et al. (2007), an indication that the minimum gap ratio needed for the onset of streamwise varies with respect to Re .

They also observed that when the gap ratio G , which they denote as L/D in their paper, increases from 3 to 4, the maximum amplitude of the lift coefficient increases by almost threefold. This can be attributed quite easily to the current vortex pair shed by the upstream cylinder. The downstream cylinder immediately disturbs the pair shed from the upstream cylinder when $G = 3$. The lift coefficient increases by about a factor of 3 when this immediate disturbance diminishes at $G = 4$. The visualisation of three-dimensional (3D) vorticity isocontours enables us to quickly establish this link vis-à-vis the lift coefficient signal. The authors use of CFD made this possible.

A similar study in the order of magnitude $Re \sim O(10^2)$ by Zhao and Lu (2018) particularly highlighted the immense utility of CFD as a tool to research SVIV or flow around a cruciform in general. They computed the sectional lift coefficient along the upstream cylinder, and the time history of this sectional lift coefficient revealed two different modes of vortex shedding, namely, parallel and K-shaped. They also paid attention to the local flow patterns that vary along the length of the upstream cylinder such as the trailing vortex flow, necklace vortex flow and flow in the small gap (denoted as SG flow). The discontinuities in the phase angle of the sectional lift coefficient along the upstream cylinder seems to suggest the inadequateness of attributing the lift coefficient to streamwise vortex shedding alone, particularly when Karman vortex streamlines were also observed some distance away from the junction of the cruciform. Shirakashi

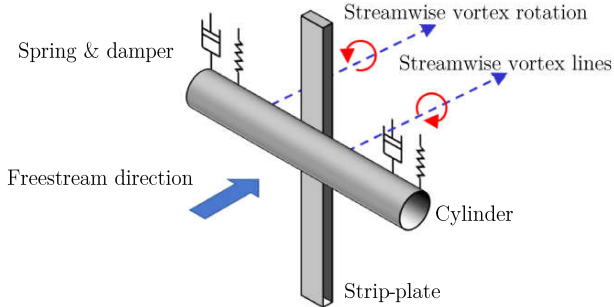


Figure 1: A schematic of the circular cylinder-strip plate cruciform system. Alternate shedding of the streamwise vortices create the alternating lift that drives the vibration of the cylinder.

et al. (1989) also made a similar observation in their experimental work. This leads us to hypothesise that the lift signal is more appropriately viewed as the streamwise-Karman vortex-induced composite lift signal. However, we could not find studies that took this viewpoint and worked out its implication on power generation in their investigation of SVIV.

The objectives of this study are thus threefold: (1) to take a closer look at the amplitude and frequency response of a circular cylinder-strip plate cruciform, especially in reduced velocity (U^*) ranges where the transition from KVIV to SVIV occurs, (2) to demonstrate the compositeness of the lift signal of an SVIV system and establish the difference between the lift signal characteristics in the KVIV and SVIV regime and (3) to shed light on how the contribution from the Karman and streamwise components of lift changes as we increase U^* after the onset of SVIV and predict how much improvement in the power generation can be anticipated if we are able to unify the lift amplitude contributions due to Karman and streamwise vortex shedding. Here, $U^* = U/f_n D$, with U , f_n and D being the freestream velocity, natural frequency of the system and the diameter of the circular cylinder respectively. The following §2 details the methodology we employ to conduct this study. We present and discuss our results in §??, §??, and §??. We describe our conclusions in §8.

2. Methodology

2.1. Problem geometry

The geometrical setup for this study builds on the work of Maruai et al. (2017, 2018) who studied both experimentally and numerically the FIM of a square cylinder with a downstream flat plate. Their simulation results are in good agreement with their own experiment, and with the experimental results of Kawabata et al. (2013), in the Reynolds number range $3.6 \times 10^3 < Re < 12.5 \times 10^3$. This is well within the Reynolds number studied in this work, i.e. $1.1 \times 10^3 < Re < 14.6 \times 10^3$.

Our $x - y$ plane fundamentally follows the dimensions used in Maruai et al. (2017, 2018), except for the cylinder shape, which in this study is circular, and the $20D$ distance to the outlet is measured from the downstream face of the

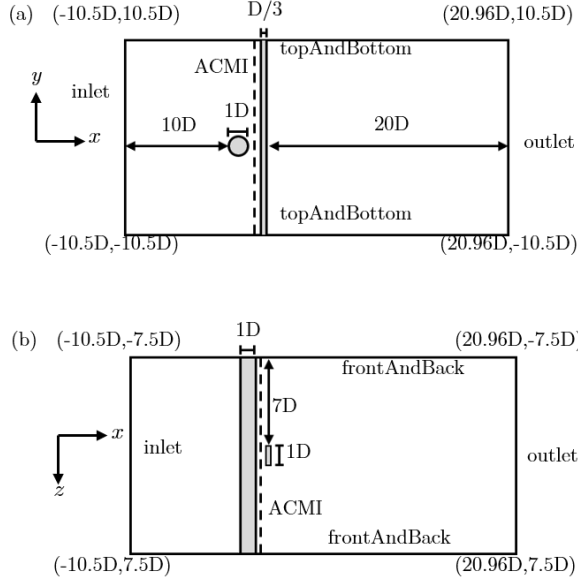


Figure 2: Problem geometry and coordinate system used. Figure 2a shows the side view of the simulation domain (cross-section perpendicular to the freestream) while Fig. 2b shows the top view of the simulation domain (cross-section parallel to the freestream). Note that the gap ratio G between the cylinder and the strip plate is $0.16D$, and the arbitrarily coupled mesh interface (ACMI) patch is located midway through the gap, i.e., $0.08D$ downstream from the trailing edge of the cylinder.

strip-plate. This is shown in Fig. 2. We chose the cylinder-plate gap G to be $0.16D$, as Koide et al. (2013) has shown that this gap size sustains the highest SVIV amplitude over the widest range of U^* , in comparison to other gap sizes.

As the problem geometry is explicitly three-dimensional (3D), the $x - y$ plane is extruded in the z direction, thus obtaining a 3D domain. As can be seen in Fig. 2, the circular cylinder extends from $z/D = 7.5$ to $z/D = -7.5$, while the strip-plate extends from -10.5 to $y/D = 10.5$. The z -direction extent is set as $z/D = \pm 7.5$ is already more than twice the spanwise reach of the streamwise vortex, thus sufficient for the vortices to materialise in our numerical solution. To compare, the spanwise extent of the numerical study by Deng et al. (2007), is $z/D = \pm 6$ and the spanwise extents of experiments by Nguyen et al. (2012) and Koide et al. (2013) are $z/D = \pm 5$.

2.2. Numerical method

The objectives of our study necessitate the solution of the continuity, and 3D unsteady Reynolds averaged Navier-Stokes (3D URANS) equations. We achieve this by using OpenFOAM, an open-source computational fluid dynamics (CFD) platform written in C++. Specifically, we work to solve the following continuity and URANS equations.

$$\frac{\partial U_i}{\partial x_i} = 0, \quad (1)$$

$$\frac{\partial U_i}{\partial t} + U_j \frac{\partial U_i}{\partial x_j} = -\frac{1}{p} \frac{P}{x_i} + \frac{\partial}{\partial x_j} \left(2\nu S_{ij} - \overline{u'_j u'_i} \right). \quad (2)$$

The symbols U , x , t , ρ , P , ν , S , and u' are the mean component of velocity, spatial component, time, density, pressure, kinematic viscosity, mean strain rate and the fluctuating component of velocity, respectively. The mean strain rate S_{ij} is given by

$$S_{ij} = \frac{1}{2} \left(\frac{\partial U_i}{\partial x_j} + \frac{\partial U_j}{\partial x_i} \right). \quad (3)$$

This study employs the Spalart-Allmaras turbulence model to approximate the Reynolds stress tensor $\tau_{ij} = \overline{u'_j u'_i}$. This turbulence model has been shown to produce results that agree reasonably well with experiments in similar flow-induced motion (FIM) studies (Ding et al., 2015a,b). We use the Boussinesq approximation to relate the Reynolds stress tensor to the mean velocity gradient

$$\tau_{ij} = 2\nu_T S_{ij}, \quad (4)$$

where ν_T represents the kinetic eddy viscosity. ν_T is, in turn, a function of $\tilde{\nu}$ and f_{v1} , while f_{v1} is a function of χ and c_{v1} , and χ a function of $\tilde{\nu}$ and ν , as shown in Eq. 5.

$$\nu_T = \tilde{\nu} f_{v1}, \quad (5a)$$

$$f_{v1} = \frac{\chi^3}{\chi^3 + c_{v1}^3}, \quad (5b)$$

$$\chi = \frac{\tilde{\nu}}{\nu}. \quad (5c)$$

Here, $\tilde{\nu}$ serves to mediate the turbulence model and dictates how $\tilde{\nu}$ is conserved.

$$\begin{aligned} \frac{\partial \tilde{\nu}}{\partial t} + U_j \frac{\partial \tilde{\nu}}{\partial x_j} &= c_{b1} \tilde{S} \tilde{\nu} - c_{w1} f_w \left(\frac{\tilde{\nu}}{D} \right)^2 \\ &+ \frac{1}{\sigma} \left\{ \frac{\partial}{\partial x_j} \left[(\nu + \tilde{\nu}) \frac{\partial \tilde{\nu}}{\partial x_j} \right] c_{b2} \frac{\partial \tilde{\nu}}{\partial x_i} \frac{\partial \tilde{\nu}}{\partial x_i} \right\} \end{aligned} \quad (6)$$

c_{b1} , c_{b2} , and c_{v1} are constant with values 0.1335, 0.622 and 7.1 respectively. c_{w1} is given by

$$c_{w1} = \frac{c_{b1}}{\kappa} + \frac{1 + c_{b2}}{\sigma}, \quad (7)$$

where additional constants κ and σ are 0.41 and 2/3 respectively. f_w , on the other hand, is given by

$$f_w = g \left(\frac{1 + c_{w3}^6}{g^6 + c_{w3}} \right)^{\frac{1}{6}}. \quad (8)$$

Here, $c_{w3} = 2$ while g is given by

$$g = r + c_{w2} (r^6 - r), \quad (9)$$

where r is

$$r = \min \left(\frac{\tilde{v}}{\tilde{S}\kappa^2 d^2}, 10 \right), \quad (10)$$

Additionally, \tilde{S} is

$$\tilde{S} = \Omega + \frac{\tilde{v}}{\kappa^2 d^2} f_{v2}, \quad (11)$$

where Ω and d are the magnitude of vorticity and the distance from the mesh nodes to the nearest wall, respectively.

Finally, f_{v2} is

$$f_{v2} = 1 - \frac{\chi}{1 + \chi f_{v1}}. \quad (12)$$

We solve these equations numerically using the PIMPLE algorithm, which combines the transient solver PISO with the steady-state solver SIMPLE for improved numerical stability.

2.3. Dynamic mesh motion

In this study, the cylinder in VIV moves perpendicular to the free stream direction. The motion unavoidably distorts the mesh around it, degrading important mesh metrics such as non-orthogonality and skewness. However, we can diffuse the mesh deformation to the neighbouring nodes as per the following Laplace equation,

$$\nabla \cdot (\gamma \nabla u) = 0. \quad (13)$$

Here, u represents the mesh deformation velocity and γ is displacement diffusion. We chose $\gamma = 1/l^2$, where l is the cell centre distance to the nearest cylinder edges. We implement the GAMG linear solver with the Gauss-Seidel smoother to solve Eq. 13. The dynamic mesh algorithm then updates the mesh node positions according to the following equation.

$$x_{\text{new}} = x_{\text{old}} + u\Delta t \quad (14)$$

The solver resumes the solution of Eqs. 1 and 2 once the mesh node positions are updated.

Another dynamic mesh handling technique used in this study is the arbitrarily coupled mesh interface (ACMI) that allows non-conforming meshes to slide over another, thus preserving the mesh quality around a moving object. The tiny gap between the cylinder and strip-plate, limits our ability to diffuse the mesh deformation to the surrounding space. ACMI is thus implemented at the centre of the gap between the circular cylinder and the strip-plate, as shown in Fig. 2, to circumvent this problem. This method has been successfully implemented in the works of Ding et al. (2015b); Zhang et al. (2018), preserving the quality of their mesh and controlling their Courant-Friedrichs-Lowy (CFL) number.

2.4. Open flow channel experiment

We set up an experimental rig to validate our numerical results at reduced velocity $U^* = 22.7$. We chose $U^* = 22.7$ because that value of U^* is where the vibration-driving mechanism is known to transit from Karman to streamwise vortex shedding (Koide et al., 2013). The experimental rig consists of a closed-loop open channel circuit based on the water tunnel used by Nguyen et al. (2012), shown in Fig. 3. The cross-section of our test section is a square with sides 100 mm in length. The test section is 1500 mm long.

The system for providing elastic support and damping to the circular cylinder follows closely those used by Kawabata et al. (2013) and Koide et al. (2013, 2017), which can be summarised as follows. The stiffness coefficient k of the plate spring is determined through a simple weight versus displacement test (Sun et al., 2016), at various active lengths of the spring. This provides a calibration curve of stiffness coefficient, k against plate spring length, l . We can

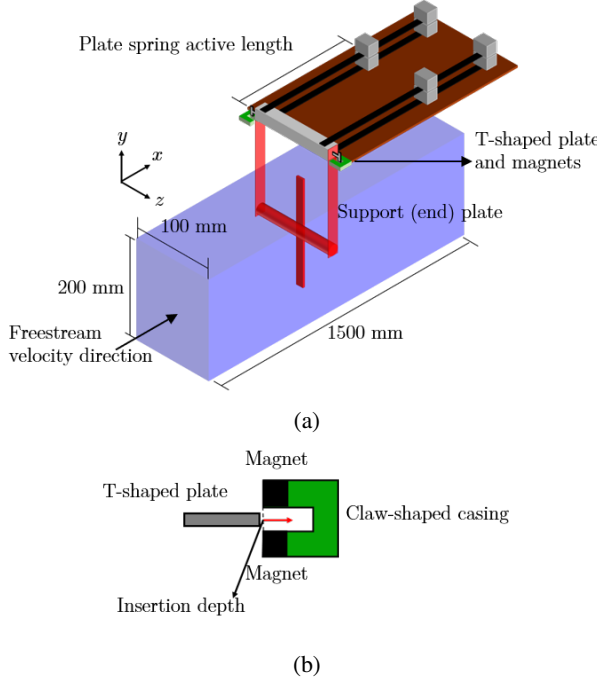


Figure 3: A schematic of our experimental setup. Figure 3a presents a 3D schematic of the experimental rig while Fig. 3b shows an enlarged schematic of the damping system.

then adjust the length of the plate spring to obtain the desired value for k .

On the other hand, the damping of the system is adjusted using T-shaped aluminium plates fixed at either end of the cylinder endplate, and a pair of neodymium magnets contained in a claw-shaped casing. The further the T-shaped plate is pushed into the opening of the claw, the denser the magnetic field it needs to cut through during motion, thus dissipating more energy. We then calibrate the damping produced at various depths at which the T-shaped plate is pushed into the casing, via free-decay tests of the cylinder in still water. The procedure for conducting free-decay tests are detailed in Raghavan (2007).

Flow inside the open channel is driven by a 3.728 kW (5 hp) centrifugal pump, controlled using a voltage controller. The input voltage for the centrifugal pump is calibrated against the centreline velocity of the test section, 750 mm from the inlet, i.e. mid-length of the test section. We show this schematically in Fig. 4. Here, we define the centreline of the test section as the line 50 mm from the bottom and 50 mm from either of the sidewalls of the test section. We placed the cylinder in the same position during experimental runs. The centreline velocity U_{cent} is measured using an acoustic Doppler velocimeter (ADV), sampling at 200 Hz. The resulting calibration curve is applicable for determining U_{cent} at input voltages $30 < V_{\text{in}}(\text{V}) < 100$. We measured the turbulence intensity along the centreline to be about 5%.

We obtained the time history for cylinder displacement, y , by using a video camera pointed normal to the cylinder endplate. We placed a visual marker on the endplate, and the motion of the marker captured by the camera is analysed

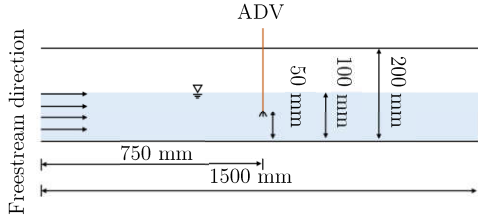


Figure 4: Side view of the open flow channel, in schematic form. Also, key dimensions of the experimental setup. The acoustic Doppler velocimeter (ADV) is placed at the same location where the cylinder is located during experimental runs.

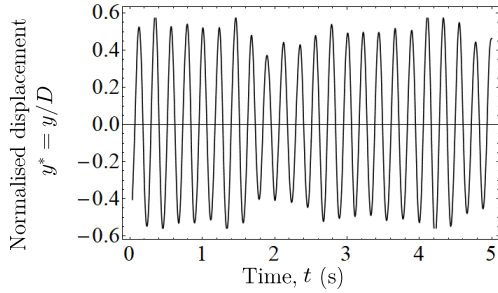


Figure 5: A sample of the time history for cylinder displacement from a test run of our experimental setup. The value of reduced velocity is $U^* = 22.7$.

using *Tracker*: a motion analysis tool built on the Open Source Physics Java framework. To validate our experimental setup, we tuned to the best of our ability our experimental parameters to the values used by Koide et al. (2013) and test whether we can replicate their results. Table 1 summarises the parameters in lieu of that paper.

Table 1

Summary of experimental parameters in contrast to those used in the experimental work of Koide et al. (2013).

	Current study	Koide et al. (2013)
Cylinder diameter, D (m)	0.01	0.01
Cylinder length, l_{cylinder} (m)	0.09	0.098
Strip-plate width (m)	0.01	0.01
Strip-plate length (m)	0.1	0.1
Effective mass, m_{eff} (kg)	0.162	0.174
Logarithmic damping, δ	0.178	0.24
Scruton number, Sc	9.94	7.74
System natural frequency, f_n (Hz)	4.42	4.4 to 4.79

We show a sample of the normalised displacement – $y^* = y/D$ – time series in Fig. 5. Computing the statistics of y^* and the normalised cylinder vibration frequency, $f^* = f_{\text{cyl}}/f_n$ (f_{cyl} being the vibration frequency of the cylinder), from several runs gave us a value of $y^* = 0.33 \pm 0.03$ and $f^* = 1.03 \pm 0.04$. Koide et al. (2013) obtained $y^* = 0.32$ and $f^* = 1.09$ under a similar U^* condition. We thus take this fairly successful reproduction of the results of Koide et al. (2013) as an indication of readiness for further data collection.

3. Numerical setup validation

3.1. Simple grid independency study

Numerical solutions of actual, continuous physical phenomena contain errors, or uncertainties, due to temporal and spatial discretisation. Reliance on the numerical method of investigation puts the responsibility on the user to minimise and justify the magnitude of error introduced in the solution.

While CFD users usually point towards their low Courant-Friedrichs-Lowy number to substantiate their claim of temporal convergence for their numerical solutions, researchers demonstrate the spatial convergence of their solution through either one of these methods. First, by solving the governing equations on several grids, each grid being a finer version of the previous one and showing that the quantities of interest are approximately the constant on all grids tested. One then chooses the mesh with a medium resolution to use in the subsequent data collection (Wu, 2011; Ding et al., 2013, 2015a, 2019).

3.2. Grid independency study via Richardson extrapolation and grid convergence index

Like the first, the second method solves the governing equations on successively finer grids. However, instead of arguing that one obtains similar results on all the grids, the investigator checks whether the quantities of interest tend towards value, as one solves the governing equation on successively finer grid resolutions (Richardson and Gaunt, 1927; Stern et al., 2001). This method, of checking for convergence pays attention not only on the presumed converged value but also on the trend of convergence. Literature that employ this method impose a monotonic convergence condition (Stern et al., 2001; Mat Ali et al., 2011; Ali et al., 2012; Maruai et al., 2018) on their quantities of interest, adding an extra layer of confidence in the final form of their spatial discretisation.

Additionally, this method allows for a quantitative description of the degree of convergence through the grid convergence index (GCI). Let $f_1, f_2, f_3, \dots, f_k$ denote the quantity of interest obtained from several grids. A larger subscript indicates a coarser grid, thus, f_1 denotes the finest while f_k denotes the coarsest grid. Let the difference between successive solutions be $\epsilon_{2,1}, \epsilon_{3,2}, \epsilon_{4,3}, \dots, \epsilon_{n,n-1}$, where $\epsilon_{2,1} = f_2 - f_1$, $\epsilon_{3,2} = f_3 - f_2$ and so on. Then, the GCI is defined as

$$\text{GCI}_{i+1,i} = F_s \frac{|\epsilon_{i+1,i}|}{f_i (r^p - 1)} \times 100\%, \quad (15)$$

where F_s , f_i and r^p denotes the safety factor ($= 1.25$), quantity of interest and the refinement ratio, r , between successive grids raised to the order of accuracy of the series of solution, p . We refer the reader to Stern et al. (2001); Langley Research Centre (2018) for a more detailed discussion on r^p .

We can estimate what the solution approaches as the grid size approaches zero by using the p^{th} method. Briefly, we compute the generalised Richardson extrapolation of the quantity of interest as follows.

$$f_{\text{RE}} = f_1 + \frac{f_1 - f_2}{r^p - 1}, \quad (16)$$

where f_{RE} is the Richardson extrapolation of the quantity of interest. Using f_{RE} to estimate the limit of the monotonically convergent series of f_i , we can determine the percentage difference of our solution on our finest grid from this limit as

$$E_i = \frac{f_i - f_{\text{RE}}}{f_{\text{RE}}} \times 100\%. \quad (17)$$

Table 2 summarises the result of our grid independency study for the SVIV reduced velocity of $U^* = 22.7$. We identified three quantities central to the investigation of fluid-structure phenomena, especially the flow-induced vibration of a circular cylinder. They are the vibration amplitude, vibration frequency and lift coefficient of the cylinder. We solve the governing equations on three grids which are numbered 1 for the finest, 2 for the medium and 3 for the coarsest, shown in Fig. 6. If we let v_i be the volume of the i^{th} cell in the grid and N be the total number of cells in the domain, then, the average cell size is

$$h = \frac{1}{N} \left[\sum_{i=1}^N v_i \right]^{1/3}, \quad (18)$$

and the normalised average cell size is hence

$$h/D = \frac{1}{ND} \left[\sum_{i=1}^N v_i \right]^{1/3}. \quad (19)$$

Both y_{RMS}^* and Cl_{RMS} starts at an initial value smaller than their Richardson extrapolations, f_{RE} , before approaching it as we decrease the average cell size, h . This similar trend can perhaps be attributed to the causal relationship between the lift coefficient and vibration amplitude. The lift drives and sustains the vibration, hence a small lift produces a small vibration, and when the lift amplitude becomes higher, so too does the vibration amplitude. The vibration frequency, on the other hand, starts at a value larger than its f_{RE} before approaching f_{RE} .

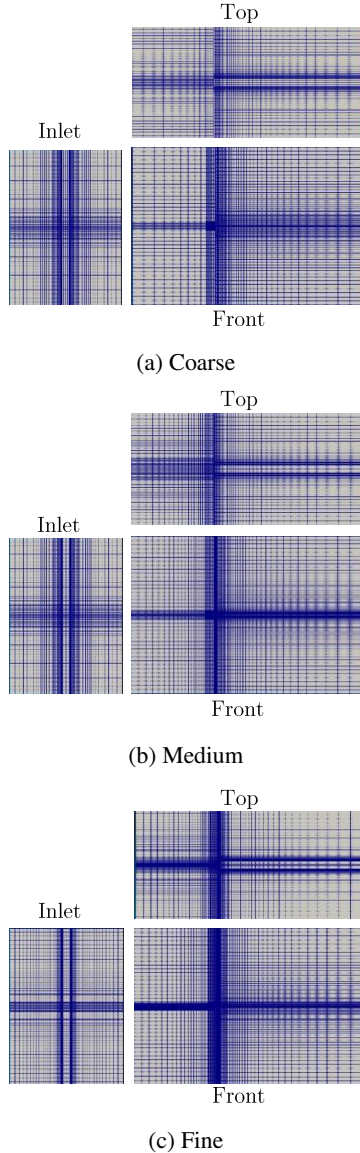


Figure 6: Three meshes used in the grid convergence study. Figures 6a, 6b and 6c show the coarse, medium and fine meshes viewed perpendicular to three main viewing positions: from the inlet, the top and the front, which is looking directly at the cylinder end.

The quantity Cl_{RMS} experiences the most significant drop in GCI as we refine the grid. The GCI is close to one-third (30.92%) as we refine the grid from coarse to medium with a refinement ratio of 1.376. The refinement ratio is calculated by dividing the number of cells in one grid with the next one down the refinement line. Following the grid numbering convention explained previously, dividing the number of cells in the fine grid (grid 1) with the number of cells in the medium grid (grid 2) gives us the refinement ratio from medium to fine, or $r_{2,1}$. Similarly, dividing the number of cells in the medium grid (grid 2) with the number of cells in the coarse grid (grid 3) gives us the refinement

ratio from coarse to medium, or $r_{3,2}$. We can generalise this to i -number of grids as follows.

$$r_{i+1,i} = \frac{S_{\text{grid},i+1}}{S_{\text{grid},i}}, \quad (20)$$

where $S_{\text{grid},i}$ denotes the total number of cells in the i^{th} grid. The GCI of Cl_{RMS} drops further to 1.63% as the mesh is refined more with a refinement ratio of 1.304.

The GCI for y_{RMS}^* also drops by one order of magnitude as can be seen by comparing $\text{GCI}_{3,2}$ with $\text{GCI}_{2,1}$. Again, this similar trend of improvement points to the causal relationship between lift and displacement of the cylinder. The GCI for f^* , however, drops by approximately a factor of 6 instead of one order of magnitude, unlike the GCIs of y_{RMS}^* and Cl_{RMS} .

Table 2
Summary of grid independency study.

Parameter/ metric	Cl_{RMS}	$y_{\text{RMS}}^* = y^*/D$	$f^* = f_{\text{cyl.}}/f_n$
f_{RE}	0.262	0.369	0.969
f_1	0.2598	0.3687	0.9695
f_2	0.2430	0.3588	0.9740
f_3	0.0805	0.2374	1.0220
$ \epsilon_{2,1} $	0.02	0.01	0.004
$ \epsilon_{2,1} $	0.16	0.12	0.48
$R = \epsilon_{2,1} / \epsilon_{2,1} $	0.10	0.08	0.094
$\text{GCI}_{3,2}$	30.92	6.00	0.64
$\text{GCI}_{3,2}$	1.63	0.52	0.10

We provide visual representations of the convergent Cl_{RMS} , y_{RMS}^* and f^* series in Figs. 7, 8 and 9. Note how the quantity of interest is very close to its Richardson extrapolation at the fine grid (grid 1) for all Cl_{RMS} , y_{RMS}^* and f^* . This implies that the fine grid already provides adequate spatial discretisation for the problem we are studying, and further refinements, while able to nudge our solutions even closer to the limit that is the Richardson extrapolation, may not be optimal in terms of usage of computational resources. Values of y_{RMS}^* and f^* at the fine grid already fall within experimental uncertainty as evidenced by our measurement in §2.4 and the work by Koide et al. (2013). Hence, all succeeding numerical data are gathered from the fine grid.

4. Streamwise vortex-induced vibration regime

We begin our exploration with the case of 90° and 67.5° .

5. Dual mode suppression regime

We then continue our exploration with 45° .

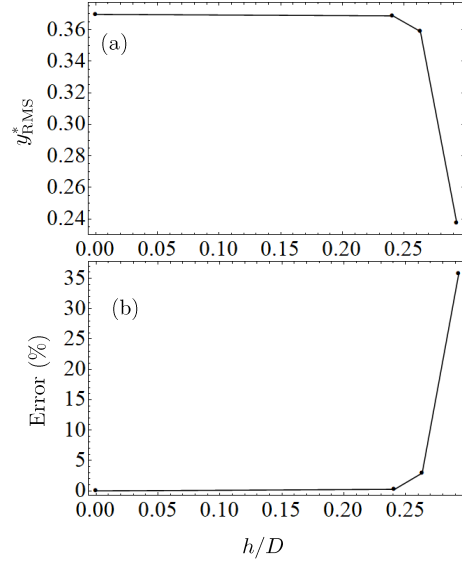


Figure 7: The convergence diagram for y^*_{RMS} . Figure 7a shows how y^*_{RMS} converges close to the Richardson extrapolation value while Fig. 7b shows how the error (difference between the value obtained from a particular mesh and the Richardson extrapolation) decreases with decreasing grid spacing.

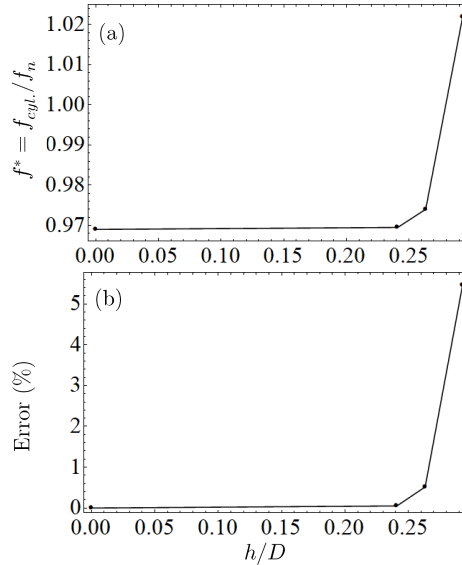


Figure 8: The convergence diagram for f^* . Figure 8a shows how f^* converges close to the Richardson extrapolation value while Fig. 8b shows how the error (difference between the value obtained from a particular mesh and the Richardson extrapolation) decreases with decreasing grid spacing.

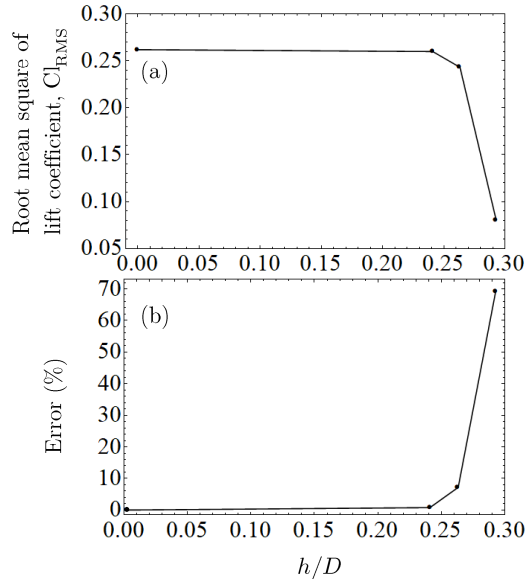


Figure 9: The convergence diagram for Cl_{RMS} . Figure 9a shows how Cl_{RMS} converges close to the Richardson extrapolation value while Fig. 9b shows how the error (difference between the value obtained from a particular mesh and the Richardson extrapolation) decreases with decreasing grid spacing.

6. Enhanced Karman vortex-induced vibration regime

7. Power characteristic in $\alpha - U^*$ parameter space

8. Conclusions

In this study, we numerically investigated the temporal evolution of the lift coefficient and cylinder displacement signals of an elastically supported cruciform system in the range $1.1 \times 10^3 < Re < 14.6 \times 10^3$, or $2.3 < U^* < 29.5$. Our circular cylinder diameter is 10 mm and the natural frequency of the system is 4.4 Hz. Validation of key numerical results was made experimentally in a custom-built open flow channel, using a cruciform system whose parameters were tuned as close as possible to the quantities used in the numerical study. Decomposing the lift coefficient signal in the SVIV regime ($15.9 \leq U^* \leq 29.5$) using EEMD allows us to see that the complexity of the lift coefficient signal as being caused by the superposition of two dominant components of lift. One due to the shedding of Karman and the other due to the shedding of streamwise vortices. The former has a frequency close to the vortex shedding frequency of Karman vortex from a smooth, isolated circular cylinder, while the latter has a mean frequency close to f_n . Application of the Hilbert-Huang transform on the dominant component of cylinder displacement – and the component of lift most correlated to it – allows for the computation of the instantaneous phase lag between lift and cylinder displacement. The time-averaged phase lag revealed five “branches” of vibration, among which is the initial branch of SVIV at $U^* = 18.2$, which has never been identified before in the literature. We also computed the instantaneous frequency of

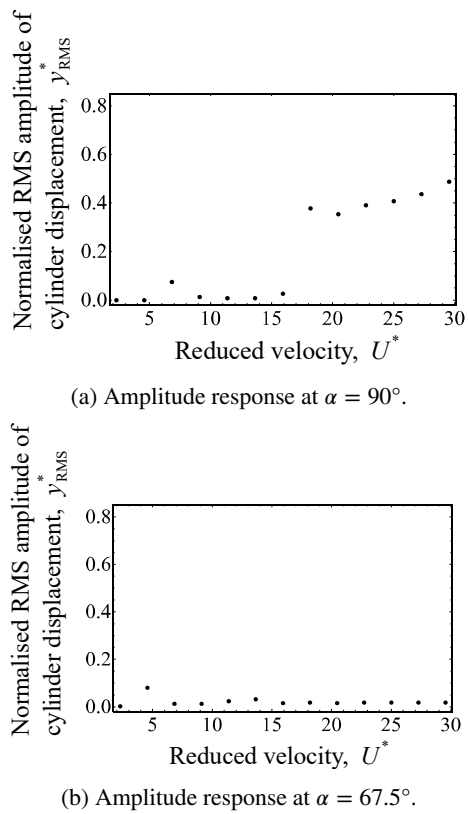


Figure 10: Evolution of the normalised RMS amplitude of cylinder displacement y_{RMS}^* , with respect to reduced velocity U^* , in the streamwise vortex-driven vibration regime.

the lift coefficient, thus revealing the loss of periodicity and self-similarity in the lift coefficient signal as the system enters the SVIV regime. Estimation of power from our results show that the root-mean-square mechanical and fluid power computed from our experimental and numerical work agree to varying degrees depending on U^* with data from similar studies in the literature. Finally, we estimated that the root-mean-square fluid power can potentially be increased close to a factor of 2 within $18.2 \leq U^* \leq 22.7$ and close to a factor of 3 when $25.0 \leq U^* \leq 29.5$. We base this estimation on the premise of redirecting the contribution to the root-mean-square amplitude of total lift from Karman vortex shedding, towards the streamwise component of lift alone.

CRediT authorship contribution statement

Ahmad Adzlan: Conceptualisation, Methodology, Software, Validation, Formal analysis, Investigation, Data curation, Writing - Original draft preparation, Visualisation. **Mohamed Sukri Mat Ali:** Conceptualisation, Methodology, Resources, Writing - Review & Editing, Supervision, Project administration, Funding acquisition. **Sheikh Ahmad Zaki:** Resources, Writing - Review & Editing.

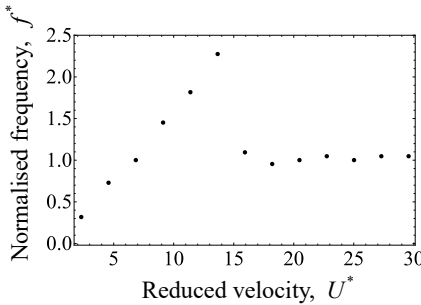
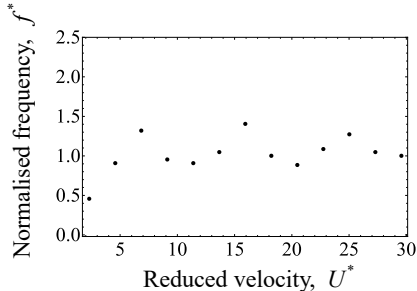
(a) Tilt angle $\alpha = 90^\circ$.(b) Tilt angle $\alpha = 67.5^\circ$.

Figure 11: Evolution of the normalised cylinder displacement frequency, f^* , with respect to reduced velocity U^* , in the streamwise vortex-driven vibration regime.

References

- Ali, M.S.M., Doolan, C.J., Wheatley, V., 2012. Low Reynolds number flow over a square cylinder with a detached flat plate. International Journal of Heat and Fluid Flow 36, 133–141. URL: <http://dx.doi.org/10.1016/j.ijheatfluidflow.2012.03.011>, doi:10.1016/j.ijheatfluidflow.2012.03.011.
- Bernitsas, M., Raghavan, K., 2008. Reduction/suppression of VIV of circular cylinders through roughness distribution at $8 \times 10^3 < Re < 1.5 \times 10^5$, in: Proceedings of the International Conference on Offshore Mechanics and Arctic Engineering - OMAE.
- Bernitsas, M.M., Ben-Simon, Y., Raghavan, K., Garcia, E.M.H., 2009. The VIVACE Converter: Model Tests at High Damping and Reynolds Number Around 10^5 . Journal of Offshore Mechanics and Arctic Engineering 131. URL: <http://offshoremechanics.asmedigitalcollection.asme.org/article.aspx?articleid=1472649>, doi:10.1115/1.2979796.
- Bernitsas, M.M., Raghavan, K., Ben-Simon, Y., Garcia, E.M.H., 2008. VIVACE (Vortex Induced Vibration Aquatic Clean Energy): A New Concept in Generation of Clean and Renewable Energy From Fluid Flow. Journal of Offshore Mechanics and Arctic Engineering 130, 041101. URL: <http://www.scopus.com/record/display.url?eid=2-s2.0-56749179917&origin=resultslist&sort=plf-f&src=s&st1=A+new+concept+in+generation+of+clean+and+renewable+energy+from+fluid+flow&sid=620865A71FAF26768C42655E1E8BC194.aXczxbyuHHiXgaIW6Ho7g:230&sot=b&sdt=b&h>, doi:10.1115/1.2957913.
- Deng, J., Ren, A.L., Shao, X.M., 2007. The flow between a stationary cylinder and a downstream elastic cylinder in cruciform arrangement. Journal of Fluids and Structures 23, 715–731. URL: <https://www.sciencedirect.com/science/article/pii/S0889974606001472>, doi:10.1016/J.JFLUIDSTRUCTS.2006.11.005.
- Ding, L., Bernitsas, M.M., Kim, E.S., 2013. 2-D URANS vs. experiments of flow induced motions of two circular cylinders in tandem with

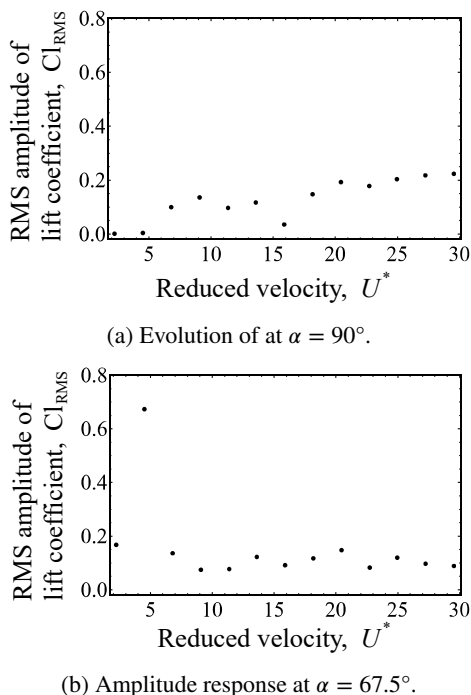


Figure 12: Evolution of the RMS amplitude of lift coefficient Cl_{RMS} , with respect to reduced velocity U^* , in the streamwise vortex-driven regime.

passive turbulence control for 30,000. Ocean Engineering 72, 429–440. URL: <http://www.sciencedirect.com/science/article/pii/S0029801813002448?via%20ihub>, doi:10.1016/J.OCEANENG.2013.06.005.

Ding, L., Zhang, L., Kim, E.S., Bernitsas, M.M., 2015a. URANS vs. experiments of flow induced motions of multiple circular cylinders with passive turbulence control. Journal of Fluids and Structures 54, 612–628. doi:10.1016/j.jfluidstructs.2015.01.003.

Ding, L., Zhang, L., Wu, C., Mao, X., Jiang, D., 2015b. Flow induced motion and energy harvesting of bluff bodies with different cross sections. Energy Conversion and Management doi:10.1016/j.enconman.2014.12.039.

Ding, W., Sun, H., Xu, W., Bernitsas, M.M., 2019. Numerical investigation on interactive FIO of two-tandem cylinders for hydrokinetic energy harnessing. Ocean Engineering 187, 106215. URL: <https://www.sciencedirect.com/science/article/pii/S0029801819304019>, doi:10.1016/J.OCEANENG.2019.106215.

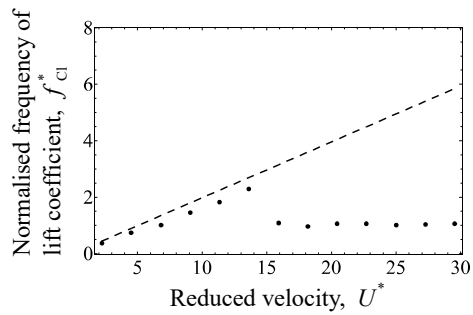
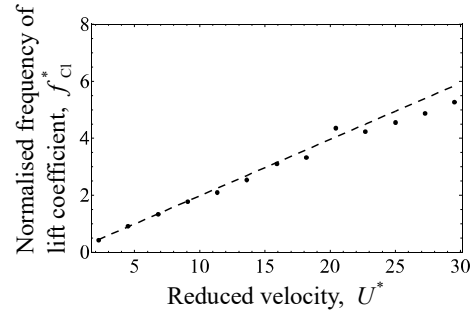
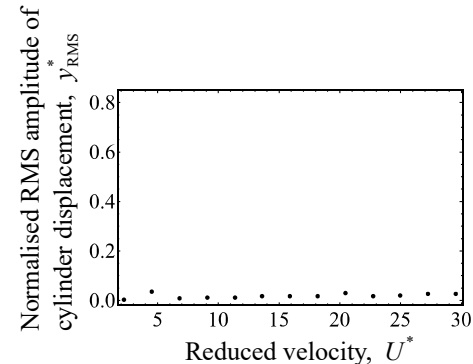
Kawabata, Y., Takahashi, T., Haginoya, T., Shirakashi, M., 2013. Interference Effect of Downstream Strip-Plate on the Crossflow Vibration of a Square Cylinder. Journal of Fluid Science and Technology 8, 647–658. doi:10.1299/jfst.8.348.

Koide, M., Kato, N., Yamada, S., Kawabata, Y., Takahashi, T., Shirakashi, M., 2007. Influence Of A Cruciform Arrangement Downstream Strip-Plate On Crossflow Vibration. Journal of Computational and Applied Mechanics 8, 135–148.

Koide, M., Ootani, K., Yamada, S., Takahashi, T., Shirakashi, M., 2006. Vortex Excitation Caused by Longitudinal Vortices Shedding from Cruciform Cylinder System in Water Flow. JSME International Journal 49, 1043–1048.

Koide, M., Sekizaki, T., Yamada, S., Takahashi, T., Shirakashi, M., 2009. A Novel Technique for Hydroelectricity Utilizing Vortex Induced Vibration, in: Proceedings of the ASME Pressure Vessels and Piping Division Conference, PVP2009-77487.

Koide, M., Sekizaki, T., Yamada, S., Takahashi, T., Shirakashi, M., 2013. Prospect of Micro Power Generation Utilizing VIV in Small Stream Based on Verification Experiments of Power Generation in Water Tunnel. Journal of Fluid Science and Technology 8, 294–

(a) Evolution of at $\alpha = 90^\circ$.(b) Amplitude response at $\alpha = 67.5^\circ$.**Figure 13:** Evolution of the normalised frequency of lift coefficient, f_{Cl}^* with respect to reduced velocity U^* in the streamwise vortex-driven regime.(a) Tilt angle $\alpha = 45^\circ$.**Figure 14:** Evolution of the normalised RMS amplitude of cylinder displacement y_{RMS}^* , with respect to reduced velocity U^* , in the region where Karman and streamwise vortex-driven vibrations are most suppressed.

308. URL: <https://www.jstage.jst.go.jp/article/jfst/8/3/8{ }294{ }articlehttp://jlc.jst.go.jp/DN/JST.JSTAGE/jfst/8.294?lang=en&from=CrossRef&type=abstract>, doi:10.1299/jfst.8.294.

Koide, M., Takahashi, T., Shirakashi, M., Salim, S.A.Z.B.S., 2017. Three-dimensional structure of longitudinal vortices shedding from cruciform two-cylinder systems with different geometries. *Journal of Visualization* , 1–11.

Langley Research Centre, 2018. Turbulence Modeling Resource. URL: <https://turbmodels.larc.nasa.gov/>.

Maruai, N.M., Ali, M.S.M., Ismail, M.H., Zaki, S.A., 2018. Flow-induced vibration of a square cylinder and downstream

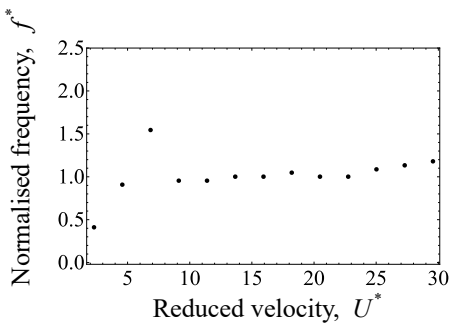
(a) Tilt angle $\alpha = 45^\circ$.

Figure 15: Evolution of the normalised cylinder displacement frequency, f^* , with respect to reduced velocity U^* , in the region where Karman and streamwise vortex-driven vibrations are most suppressed.

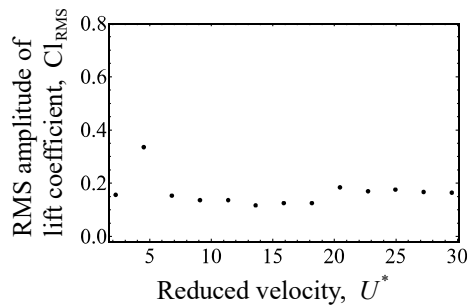
(a) Evolution of at $\alpha = 45^\circ$.

Figure 16: Evolution of the RMS amplitude of lift coefficient Cl_{RMS} , with respect to reduced velocity U^* , in the region where Karman and streamwise vortex-driven vibrations are most suppressed.

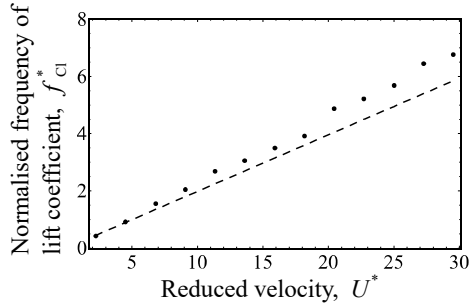
(a) Evolution of at $\alpha = 45^\circ$.

Figure 17: Evolution of the normalised frequency of lift coefficient, f_{Cl}^* with respect to reduced velocity U^* in the region where Karman and streamwise vortex-induced vibrations are most suppressed.

flat plate associated with micro-scale energy harvester. Journal of Wind Engineering and Industrial Aerodynamics 175, 264–282. URL: <https://www.scopus.com/inward/record.uri?eid=2-s2.0-85042219159&doi=10.1016/j.jweia.2018.01.010&partnerID=40&md5=2f3f62b94bb69ced3368b32e682aefc7>, doi:10.1016/j.jweia.2018.01.010.

Maruai, N.M., Mat Ali, M.S., Ismail, M.H., Shaikh Salim, S.A.Z., 2017. Downstream flat plate as the flow-induced vibration enhancer for energy harvesting. Journal of Vibration and Control , 107754631770787URL: <http://journals.sagepub.com/doi/10.1177/1077546317707877>,

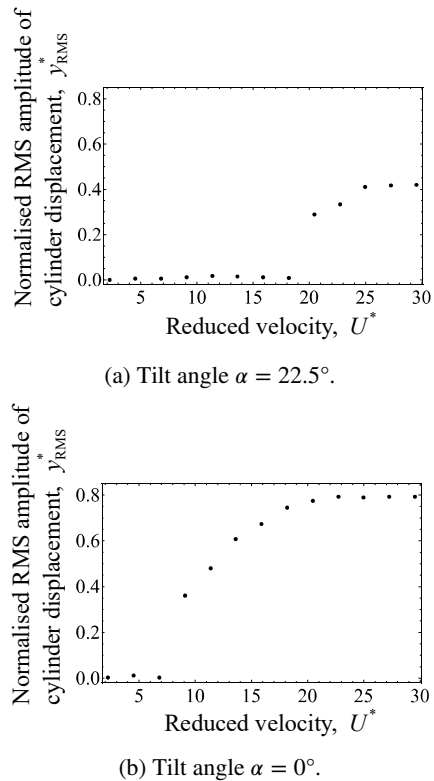


Figure 18: Evolution of the normalised RMS amplitude of cylinder displacement y_{RMS}^* , with respect to reduced velocity U^* , in the Karman vortex-driven regime.

doi:10.1177/1077546317707877.

Mat Ali, M.S., Doolan, C.J., Wheatley, V., 2011. Low Reynolds number flow over a square cylinder with a splitter plate. Physics of Fluids 23.

doi:10.1063/1.3563619.

Nguyen, T., Koide, M., Yamada, S., Takahashi, T., Shirakashi, M., 2012. Influence of mass and damping ratios on VIVs of a cylinder with a downstream counterpart in cruciform arrangement. Journal of Fluids and Structures 28, 40–55. doi:10.1016/j.jfluidstructs.2011.10.006.

Raghavan, K., 2007. Energy Extraction from a Steady Flow Using Vortex Induced Vibration. Doctoral dissertation. The University of Michigan.
URL: <http://deepblue.lib.umich.edu/handle/2027.42/55687>.

Richardson, L.F., Gaunt, J.A., 1927. The deferred approach to the limit. Philosophical Transactions of the Royal Society A doi:<https://doi.org/10.1098/rsta.1927.0008>.

Shirakashi, M., Mizuguchi, K., Bae, H.M., 1989. Flow-induced excitation of an elastically-supported cylinder caused by another located downstream in cruciform arrangement. Journal of Fluids and Structures 3, 595–607. doi:10.1016/S0889-9746(89)90150-3.

Stern, F., Wilson, R.V., Coleman, H.W., Paterson, E.G., 2001. Comprehensive approach to verification and validation of CFD simulations part 1: methodology and procedures. Journal of fluids engineering 123, 793–802.

Sun, H., Kim, E.S., Nowakowski, G., Mauer, E., Bernitsas, M.M., 2016. Effect of mass-ratio, damping, and stiffness on optimal hydrokinetic energy conversion of a single, rough cylinder in flow induced motions. Renewable Energy 99, 936–959. URL: <http://www.sciencedirect.com/science/article/pii/S0960148116306206>, doi:10.1016/j.renene.2016.07.024.

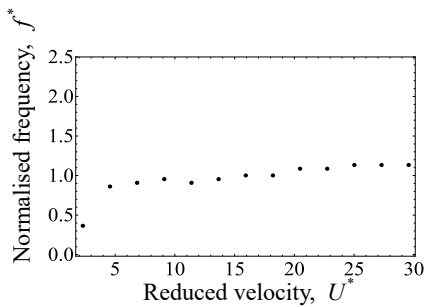
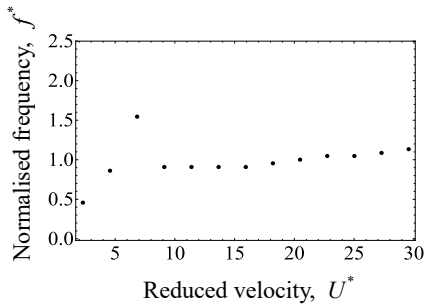
(a) Tilt angle $\alpha = 22.5^\circ$.(b) Tilt angle $\alpha = 0^\circ$.

Figure 19: Evolution of the normalised cylinder displacement frequency, f^* , with respect to reduced velocity U^* , in the Karman vortex-driven vibration regime.

Wu, W., 2011. Two-Dimensional RANS Simulation of Flow Induced Motion of Circular Cylinder with Passive Turbulence Control. Doctoral dissertation. The University of Michigan.

Zhang, B., Mao, Z., Song, B., Ding, W., Tian, W., 2018. Numerical investigation on effect of damping-ratio and mass-ratio on energy harnessing of a square cylinder in FIM. Energy 144, 218–231. URL: [https://www.scopus.com/inward/record.uri?eid=2-s2.0-85037995662&doi=10.1016%2Fj.energy.2017.11.153](https://www.scopus.com/inward/record.uri?eid=2-s2.0-85037995662&doi=10.1016%2Fj.energy.2017.11.153&partnerID=40&md5=01db7c6b6d4d44e88de7045843c7d423).

Zhao, M., Lu, L., 2018. Numerical simulation of flow past two circular cylinders in cruciform arrangement. Journal of Fluid Mechanics 848, 1013–1039. URL: https://www.cambridge.org/core/product/identifier/S0022112018003804/type/journal_article, doi:10.1017/jfm.2018.380.

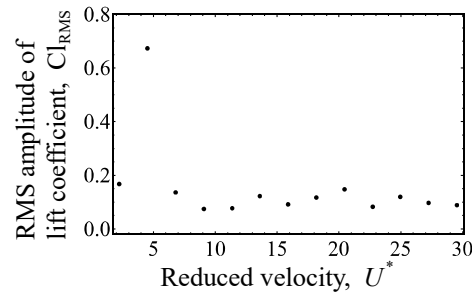
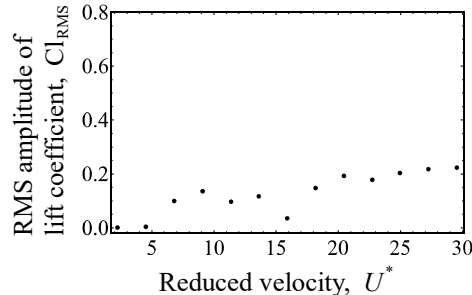
(a) Evolution of at $\alpha = 45^\circ$.(b) Evolution of at $\alpha = 45^\circ$.

Figure 20: Evolution of the RMS amplitude of lift coefficient Cl_{RMS} , with respect to reduced velocity U^* , in the Karman vortex-driven vibration regime.

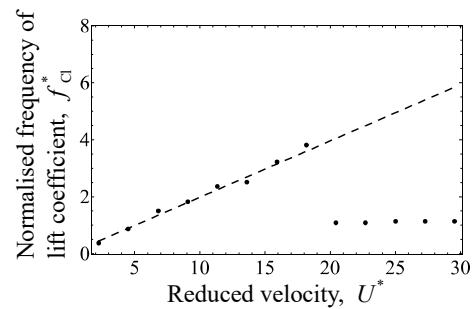
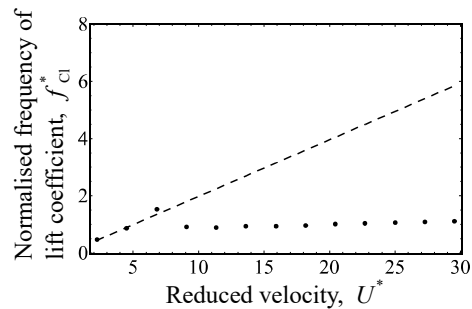
(a) Evolution of at $\alpha = 45^\circ$.(b) Evolution of at $\alpha = 45^\circ$.

Figure 21: Evolution of the normalised frequency of the lift coefficient, with respect to reduced velocity U^* in the Karman vortex-driven regime.

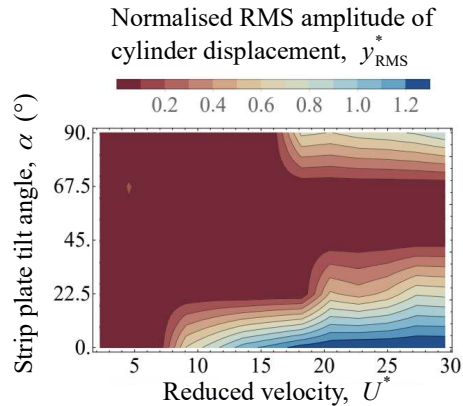


Figure 22: Isocontours describing the map of the normalised RMS amplitude of cylinder displacement, y_{RMS}^* in the cruciform angle - reduced velocity ($\alpha-U^*$) parameter space.

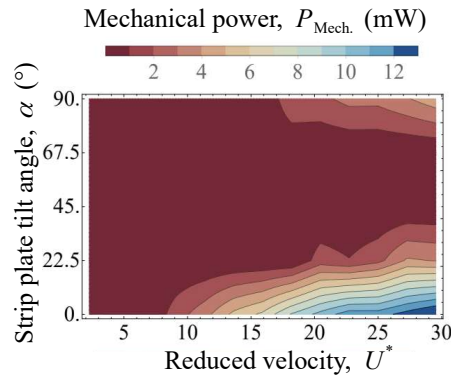


Figure 23: Isocontours describing the map of the estimated mechanical power in the cruciform angle - reduced velocity ($\alpha-U^*$) parameter space.

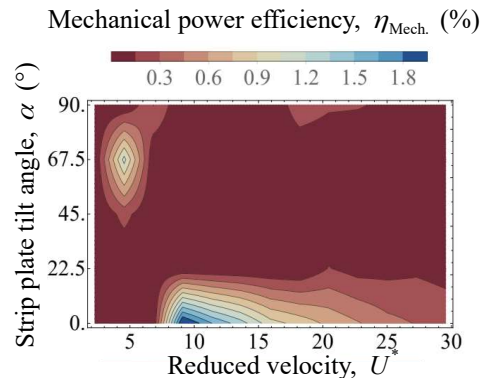


Figure 24: Isocontours describing the map of the estimated mechanical power in the cruciform angle - reduced velocity ($\alpha-U^*$) parameter space.